Petroleum Science 21 (2024) 4328–4343

Contents lists available at ScienceDirect

Petroleum Science

journal homepage: www.keaipublishing.com/en/journals/petroleum-science

Original Paper

Study on the influence factors of rock breaking by supercritical CO_2 thermal fracturing

Shao-Bin Hu [a,*], Lin Zhang [a], Yu-Kang Cai [a], Shuo-Gang Pang [a], Zheng-Yong Yan [a], Qiang Zhang [b,c]

[a] Tunnel and Underground Engineering Institute, College of Civil and Transportation Engineering, HoHai University, Nanjing, 210024, Jiangsu, China
[b] Powerchina Huadong Engineering Corporation Limited, Hangzhou, 311122, Zhejiang, China
[c] Powerchina Zhejiang Huadong Engineering Consulting Corporation Limited, Hangzhou, 311122, Zhejiang, China

ARTICLE INFO

Article history:
Received 31 October 2023
Received in revised form
24 July 2024
Accepted 29 July 2024
Available online 31 July 2024

Edited by Jia-Jia Fei and Min Li

Keywords:
Supercritical CO_2
Thermal fracturing
Phase change
Transient nonlinear flow
Multi-field coupled

ABSTRACT

At present, there is a growing demand for safe and low-pollution rock-breaking technology. The rock breaking technology of supercritical CO_2 thermal fracturing has many advantages, such as no dust noise, no explosion, high efficiency, controllable shock wave and so on. Fully considering the combustion rate of energetic materials, heat and mass transfer, CO_2 phase change and transient nonlinear flow process, a multi-field coupled numerical model of rock breaking by supercritical CO_2 thermal fracturing was established based on the existing experiments. The influence factors of CO_2 thermal fracturing process were studied to provide theoretical guidance for site construction parameters optimization. The numerical simulation results were in good agreement with the experimental observation results. The results showed that the maximum temperature of CO_2 and the growth rate of CO_2 pressure during the fracturing process would decrease accordingly with the increase of CO_2 initial pressure. But the change in CO_2 peak pressure wasn't significant. Appropriately increasing the heat source power could improve the heating and pressurization rate of CO_2 and accelerate the damage rate of rock. The relevant results were of great importance for promoting the application of rock breaking by supercritical CO_2 thermal fracturing technology.

1. Introduction

Since the 21st century, the traditional oil and gas resources in the shallow part of the earth have gradually been exhausted. Deep unconventional oil and gas resources have become the focus of attention to meet increasing demands for energy (Jiao, 2019; Song et al., 2017). Compared with the shallow space, the deep rock stratum is more dense, with high in-situ stress, low porosity and low permeability, and difficult to form complex fractures (Chen et al., 2017; Muther et al., 2022; Wang et al., 2018). Hydraulic fracturing has some disadvantages such as limited permeability enhancement capacity, few fractures, groundwater pollution and waste a lot of water (Uzun and Kazemi, 2021; Liang et al., 2017). Moreover, water-based fracturing fluids will cause damage, such as water sensitivity, the water lock effect and polymer adsorption, and clay swelling problems in shale (Zhao et al., 2019; Middleton et al., 2014). These concerns have stimulated exploration into the use of nonaqueous fracturing fluids, such as supercritical CO_2 (abbreviated as Sc-CO_2), liquefied petroleum gases (LPGs), hydroxypropyl guar gums (HPGs), liquefied natural gases (LNGs), and foam-based fracturing fluids (Kohshou et al., 2017; Li et al., 2021; Meng et al., 2019). Among them, Sc-CO_2 is considered as an ideal nonaqueous fracturing fluid due to its superior properties of liquid-like density, gas-like viscosity, low surface tension, strong compressibility and diffusibility (Zhang et al., 2016; Wang et al., 2019; He et al., 2019; Li et al., 2020). Sc-CO_2 is easy to form more complex and high-yield fracture network in the reservoir based on these characteristics (Verdon et al., 2010; Middleton et al., 2015; She et al., 2023). The ability of Sc-CO_2 to permeate rock changes the mechanical properties and pore pressure of the formation, resulting in two orders of magnitude more fractures than hydraulic fracturing (Meng and Qiu, 2018; Zhou et al., 2018; Liu et al., 2018).

Many scholars around the world are exploring Sc-CO_2 fracturing

* Corresponding author.
E-mail address: 20170037@hhu.edu.cn (S.-B. Hu).

https://doi.org/10.1016/j.petsci.2024.07.028

technology. When the pressure and temperature of CO_2 are higher than the critical pressure (7.29 MPa) and temperature (31.26 °C), CO_2 transforms into a supercritical state (Zhu et al., 2022). The results showed that the Sc-CO_2 pressure to initiate fracturing was approximately 50% lower than that of hydraulic fracturing (Zhang et al., 2020; Li et al., 2020; Ha et al., 2018). This was mainly because the viscosity of Sc-CO_2 was very low, and the viscosity was an important factor affecting the fracture initiation pressure (Ishida et al., 2016; Zhao et al., 2018; Chen et al., 2021; Liu et al., 2020). However, the low viscosity characteristic of Sc-CO_2 could also bring some negative effects.

Relevant scholars have found that the fracture width of Sc-CO_2 fracturing was narrower than that of hydraulic fracturing (Li et al., 2019; Ma et al., 2021), and it was easy to plug. This was mainly due to the problems of poor sand carrying capacity, easy sand plugging and high flow friction caused by the low viscosity of Sc-CO_2. In this case, Hu et al. (2019) proposed a new dynamic fracturing technology, namely Sc-CO_2 thermal fracturing technology. This technology used intrinsically safe heating material (energy accumulating agent) to burn in CO_2 to produce a large amount of heat energy, which produced high-pressure rock breaking effect. The whole process of dynamic fracturing with this technology could effectively expand the width of rock fractures, and increased the effect and controllability of CO_2 phase change fracturing.

Numerous scholars have conducted initial research on CO_2 fracturing technology in the past. Cai et al. (2020) designed a novel visualized experimental system of SC-CO_2 jet fracturing. In the whole experimental system, the most important unit was the high-pressure & temperature visualized vessel. The experimental results showed that there was optimal jet distance under low ambient pressure, and reducing jet distance was better for the jet fracturing under high ambient pressure. She et al. (2023) conducted the true triaxial fracturing experiments with supercritical CO_2 and slick-water. The experimental results showed that the increase in the displacement rate and the decrease in the in-situ stress difference for supercritical CO_2 fracturing was more conducive to the multi-point initiation and reorientation of the hydraulic fractures. However, the above experiments achieved an increase in fluid pressure and temperature by injecting CO_2. Slowly injecting CO_2 would generate static loads on the rock. The rock fractured when the load reached the ultimate strength of the rock. During the process of Sc-CO_2 thermal fracturing, the impact process was a dynamic loading process with higher strain rate because of the high growth rate of CO_2 pressure, which could achieve higher peak pressure and produce better fracturing effect (Hu et al., 2019). Zhou et al. (2021) found that the vibration signal of CO_2 phase change fracturing was a random non-stationary signal with no obvious high-frequency oscillation. Wang et al. (2024) designed and conducted a CO_2 fracturing experiment in a larger sealed test platform. The larger model could study the vibration characteristics in coal and rock far from the fracturing hole. The sealed test platform ensured that the test was carried out at a constant temperature. Although some achievements have been made in temperature control in this experiment, it couldn't capture the complete temperature field fluctuations throughout the entire fracturing process.

Numerical simulation has the advantages of intuitive analysis, quantification and visualization of results. Li et al. (2020) used fluid-solid coupling discrete element model (DEM) to study Sc-CO_2 fracturing. It was found that the fluid pressure in a whole fracture driven by Sc-CO_2 was uniform, while a large pressure gradient existed in a fracture induced by high-viscosity fluid. Yan et al. (2019, 2021) obtained the influence of in-situ stress deviation, coal permeability coefficient, fracturing fluid injection rate and temperature on rock fractured by Sc-CO_2 through numerical simulation. Considering the interaction between the fracturing fractures and the embedded pre-existing fractures, Wang et al. (2019) introduced an adaptive finite element–discrete element method and local remeshing strategy to simulate the propagation of fracturing fractures. However, the existing numerical models of Sc-CO_2 fracturing were pressurized by constant flow injection, and the fluid pressure was a gradually slow loading process. Their simulation methods couldn't realize the impact force caused by the instantaneous rise of fluid temperature and pressure, and also couldn't fully reflect the effects of strong nonlinear flow, heat and mass transfer process and the rapid rise of Sc-CO_2 temperature. Therefore, the motion characteristics and fracture mechanism of fluid in the process of Sc-CO_2 fracturing aren't clear at present.

In this paper, a multi-field coupled numerical model was established to solve the problems of CO_2 phase change, combustion rate of energetic materials, heat and mass transfer and transient nonlinear flow, and further reveal the mechanism of rock breaking by Sc-CO_2 thermal fracturing technology. This work is of great significance for the formation of more complex rock fracture networks.

2. Experiment of supercritical CO_2 thermal fracturing

2.1. Experimental system and sample preparation

The Sc-CO_2 thermal fracturing experimental system is mainly composed of four branch systems, namely fluid injection system, triaxial loading system, transient aerodynamic impulse system and data acquisition system, as shown in Figs. 1 and 4.

(1) Fluid injection system

The fluid injection system is composed of liquid CO_2 cylinder, double cylinder pump, air compressor and water bath circulation system. The liquid CO_2 cylinder provides liquid CO_2 with stable pressure for the double cylinder pump. The air compressor is connected with the double cylinder pump. The air compressor provides power for the double cylinder pump to pressurize and increase energy. The water bath circulation system is used to cool down and control the CO_2 in the double cylinder pump to be liquid. The double cylinder pump injects the liquid CO_2 into the cracking tube with constant flow or constant pressure.

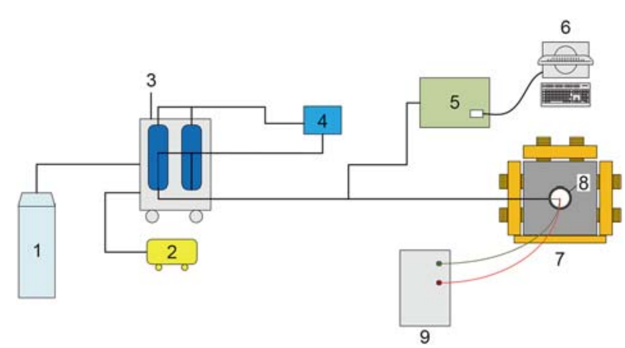

Fig. 1. CO_2 thermal fracturing experimental device.
In Fig. 1: 1-liquid CO_2 cylinder; 2-air compressor; 3-double cylinder pump; 4-water bath system; 5-eight-channel data acquisition instrument; 6-computer; 7-triaxial loading system and sample; 8-cracking tube; 9-electromagnetic induction device.

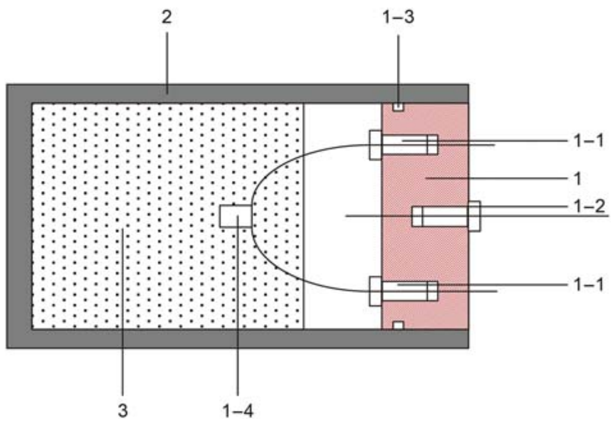

Fig. 2. Schematic diagram of the transient aerodynamic pulse device.
In Fig, 2: 1-high pressure cracking tube joint, including wire port (1–1), air inlet (1–2), gasket groove (1–3) and electromagnetic induction coil (1–4); 2-high-pressure cracking tube body; 3-energy accumulating agent.

(2) Triaxial loading system
The triaxial loading system consists of oil pressure jack, loading gasket, loading platform and three CP-900 manual oil pressure pumps. The loading platform is used to place a 200 mm × 200 mm × 200 mm cube sample, and triaxial pressure is applied to the sample through the CP-900 manual oil pressure pump. The front side of the cube sample will be prefabricated with cracking hole and cracking tube. Under the action of the fluid injection system, the liquid CO_2 with constant pressure can be introduced into the cracking tube inside the sample through the pipe.

(3) Transient aerodynamic impulse system
As shown in Figs. 2 and 3, the transient aerodynamic impulse system is composed of cracking tube, energy accumulating agent, electromagnetic induction coil, etc. The Sc-CO_2 thermal fracturing experiment uses a double cylinder pump to drive the high-pressure liquid CO_2 into the prefabricated high-pressure cracking tube and maintain it at the initial set pressure. The energy accumulating agent is a porous high energy accumulating alloy granular material (Hu et al., 2016) that forms miscible fluid with CO_2, resulting in its internal pores filled with liquid CO_2. Therefore, the heat source can be regarded as CO_2 energy accumulating miscible fluid (the mixture of energy accumulating agent particles and CO_2).

Fig. 3. Photograph of the cracking tube.

Fig. 4. Photograph of the experimental system.

(4) Data acquisition system
The data acquisition system is mainly composed of pressure sensor, eight channel data acquisition instrument and computer. The digital system is used to record the data of fluid pressure changing with time in the whole process of Sc-CO_2 thermal fracturing.

It is difficult to obtain rocks with different burial depths underground, and there are many initial micro-cracks in natural rock masses. At the same time, in order to ensure the comparability and homogeneity of the experiment, artificially made special high-strength cement was used as the experimental sample. The physical and mechanical properties of this cement were similar to those of limestone, granite, marble, etc. As shown in Fig. 5, The experimental sample was a cube with a side length of 20 cm, which was made of special high-strength cement. A cracking tube with a diameter of 4 cm and a length of 10 cm was placed in the center of the sample. The experimental sample was compact, hard and homogeneous. The basic mechanical parameters of special high-strength cement were obtained in Table 1.

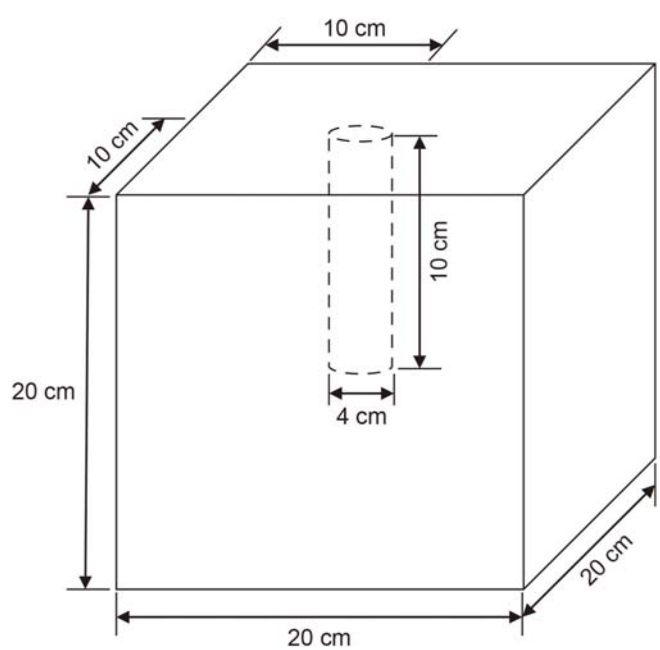

Fig. 5. Geometric diagram of special high-strength cement sample.

Table 1
Mechanical parameters of special high-strength cement sample.

Density, $kg \cdot m^{-3}$	Elastic modulus, GPa	Poisson's ratio	Tensile strength, MPa	Uniaxial compressive strength, MPa	Permeability, m^2	Porosity
2300	22	0.13	10.1	106	4.64×10^{-14}	0.07

2.2. Experimental scheme and process

The initial pressure of CO_2 determines the total amount and density of the fluid when the temperature and the volume of the container are constant. The amount of energy accumulating agent determines the heat release rate, which affects the total energy. Therefore, three groups of Sc-CO_2 thermal fracturing experiments had been carried out with the initial pressure of CO_2 and the amount of energy accumulating agent as independent variables. The triaxial pressures of 5 MPa (along the direction of cracking pipe), 6 and 8 MPa (along the vertical direction) were applied to each group to ensure that the samples wouldn't be damaged during pressure loading. The specific experimental scheme was shown in Table 2.

The process of Sc-CO_2 thermal fracturing experiment is as follows.

(1) Preliminary preparations

Poured the special high-strength cement samples before the Sc-CO_2 thermal fracturing experiment. After the cement reached the expected strength (compressive strength and elastic modulus), put the samples into the triaxial device. According to the requirements of the parameters of the energy accumulating agent, configured the corresponding chemicals for the cracking tube and set sealing measures. Turned on the circulating refrigeration function of the water bath system simultaneously to ensure that the low-temperature environment could be provided for the liquid CO_2 inside the double cylinder pump.

(2) Triaxial pressure loading

According to the experimental scheme, the special high-strength cement sample was placed in the triaxial loading system and subjected to three-dimensional pressure. In the process of pressurization, cyclic pressurization was carried out to avoid the damage of rock caused by rapid unidirectional loading.

(3) Inject liquid CO_2

Opened the liquid CO_2 cylinder and air compressor channel. Set the parameters in the double cylinder pump system according to the experimental requirements. The hydraulic double cylinder pump used the constant pressure mode to inject the liquid CO_2 into the cracking pipe. After reaching the initial CO_2 pressure, closed the air pressure valve before the electromagnetic induction device was energized.

(4) Excitation electromagnetic induction device

After the energy accumulating agent was excited by the electromagnetic induction device, it released a lot of heat. The temperature and pressure of liquid CO_2 would continue to rise, reaching the pressure limit of the cracking tube, breaking through the weak part inside the cracking tube and fracturing the cement sample. The data collected by the pressure sensor was transmitted to the multi-channel data acquisition instrument, and the change data of pressure with time was recorded simultaneously.

(5) Complete the experiment

Observed and analyzed the results of Sc-CO_2 thermal fracturing experiment.

2.3. Experimental results

As can be seen from Fig. 6(a), the peak pressure and the rising rate of the $A'A''$ section of CO_2 pressure curve increase with the increase of the amount of energy accumulating agent. This is because the energy accumulating agent is equivalent to the heat source, and the heat released will increase with the increase of the amount of energy accumulating agent. As more heat is absorbed by CO_2, the peak pressure and the rising rate of pressure will naturally increase. As shown in Fig. 6(b), the initial pressure of CO_2 has little effect on the rising rate of CO_2 pressure and peak pressure.

Three groups of typical experimental results were selected from a large number of experiments. In order to observe the crack shape more directly, the six surfaces of the sample had been pieced together to reflect the law of crack distribution. As shown in Fig. 7, the cracks formed by Sc-CO_2 thermal fracturing showed large random dispersion. As the fluid instantly generated strong kinetic energy to impact the high-strength cement, 3–4 radial cracks diffused around the fracturing hole, and the width of radial cracks was large.

3. Numerical simulation of supercritical CO_2 thermal fracturing

3.1. Numerical model structure and material parameters

Referring to the experiment of Sc-CO_2 thermal fracturing, the three-dimensional experiment was simplified into a two-dimensional model, with the same dimensions, material parameters, and initial calculation conditions as the experiment. Seen in Fig. 8, the geometric size of the model was 20 cm $\times$ 20 cm. A vertical borehole with a radius of $r = 2$ cm was arranged, and the cracking tube was placed in the borehole (area 3). The model grid was divided into triangular units, as shown in Fig. 9.

In Fig. 8, CO_2 energy accumulating miscible fluid (mixture of CO_2 and energy accumulating agent particles) was placed in area 1, and liquid CO_2 was initially in area 2. In the initial state, there were no energy accumulating agent particles in area 2, but the

Table 2
Basic experimental parameters.

Sample number	CO_2 initial pressure, MPa	Amount of energy accumulating agent, g
Sample A	15	15
Sample B	15	12
Sample C	18	12

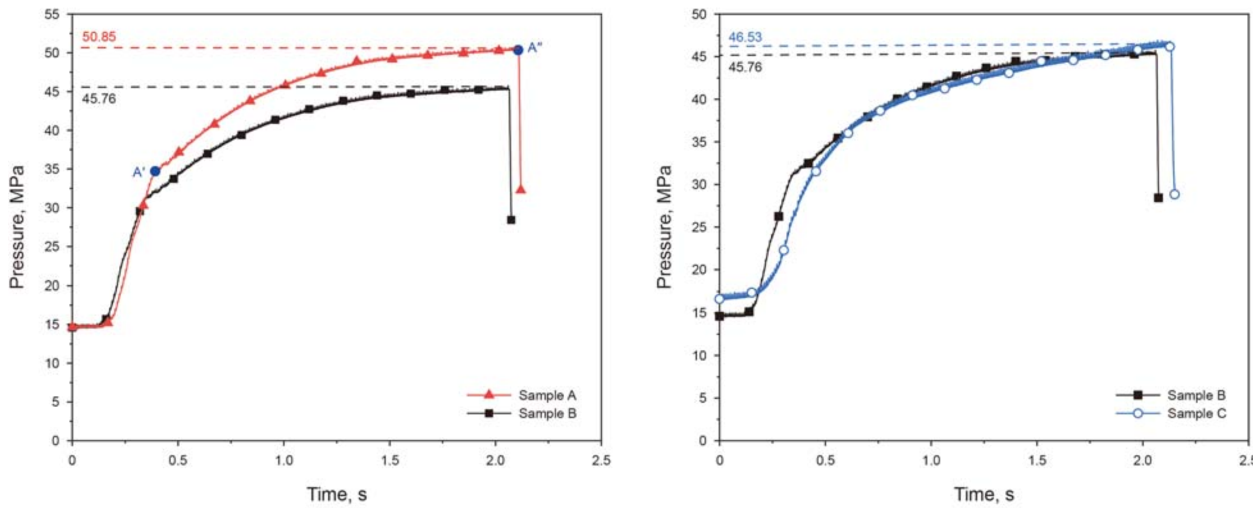

(a) CO_2 pressure curves of sample A and sample B

(b) CO_2 pressure curves of sample B and sample C

Fig. 6. Schematic diagram of CO_2 pressure curves. **(a)** CO_2 pressure curves of sample A and sample B; **(b)** CO_2 pressure curves of sample B and sample C.

concentration of energy accumulating agent particles in area 1 was very high. In the solid mechanics field, the rock bore two-way load. The horizontal and vertical displacement of the left and lower sides of the rock were limited by roll support respectively. The cracking tube was an iron container. This model directly imported the parameters of iron in the COMSOL material library, where the tensile strength of iron was 200 MPa. Since the experiment was conducted in a stationary state at room temperature, the initial temperature T_0 in the numerical simulation was set to 293.15 K, the pressure P_0 of the flow field and seepage field was set to 1 atm.

In the process of heat emission by the energy accumulating agent, the change in temperature and pressure had a great impact on the physical properties of CO_2. The physical property parameters of CO_2 at different temperatures and pressures were shown in Fig. 10, which were derived from the NIST Chemistry Webbook.

3.2. Principle of supercritical CO_2 thermal fracturing

From the whole experimental process of Sc-CO_2 thermal fracturing, there was a close coupling among rock stress field, damage field, flow field and temperature field. Firstly, there was the pressure rise process of high-temperature and high-pressure CO_2. As shown in Fig. 11, the energy accumulating agent particles would diffuse from the area with high particle concentration to the area with low concentration while burning and releasing a large amount of heat. After absorbing a large amount of heat, liquid CO_2 rapidly increased in temperature and pressure, and transformed into Sc-CO_2. This process can lead to very complex flow processes and thermal convection, involving the interaction between temperature and flow fields. Therefore, we need to consider the combined effect of convection and diffusion.

Secondly, there was a pressure relief expansion process when Sc-CO_2 broke through the cracking tube. The instantaneous expansion of Sc-CO_2 and the formation of multiple radial cracks in cement were obviously different from the normal quasi-static fracturing process of Sc-CO_2, which indicated that it is a dynamic fracturing process. Therefore, it must involve the nonlinear flow process of high-temperature and high-pressure fluid in the fracture. The process of fluid flow could cause heat convection and heat conduction, thereby affecting the distribution of temperature field. Meanwhile, the fluid pressure changed the effective stress of rock, and had an indirect effect on the process of crack propagation.

Finally, when the temperature at the crack tip was low, the Sc-CO_2 at the crack tip would expand into high energy CO_2 gas, resulting in gas wedge effect. This would change the stress intensity factor at the crack tip and make the crack continue to extend and expand. The crack propagation would affect the distribution of stress field and the flow and heat transfer of high-pressure fluid in the crack. The variation of rock stress field would change the stress intensity factor at the crack tip, affect the whole process of crack initiation, propagation and penetration, and lead to the gradual increase of rock porosity and permeability (Rummel, 1987).

The process of rock breaking by Sc-CO_2 thermal fracturing includes phase change of CO_2, heat and mass transfer, nonlinear flow in fractures, rock damage and so on, involving multiple physical fields such as flow, seepage, temperature and solid mechanics. The basic governing equations of multi-field coupling are shown in Section 3.3.

3.3. Basic governing equation of multi-field coupling

The difficulty of this numerical model was to simulate the exothermic process of the energy accumulating agent. The heat and mass transfer between the energy accumulating agent particles and CO_2 was described by using the convection-diffusion equation. The combustion rate formula of the energy accumulating agent was derived to describe the heat release process of heat source.

As the compressive strength of rock is much higher than the tensile strength, the failure mode is usually tensile failure. Under the condition of tensile stress, the fracture behavior of rock mesoscopic unit is close to elastic brittleness (Li et al., 2019). Therefore, this model adopted the maximum normal stress strength theory as the strength fracture criterion.

(1) Governing equation of rock deformation field

On the basis of the problem of dynamic elasticity, the equilibrium, geometric and constitutive equations of rock are expressed as

$$\boldsymbol{\sigma}_{ij,j} + \boldsymbol{F}_i = \rho_s \frac{\mathrm{d}^2 \boldsymbol{x}}{\mathrm{d}t^2} \quad (i,j = 1,2,3) \tag{1}$$

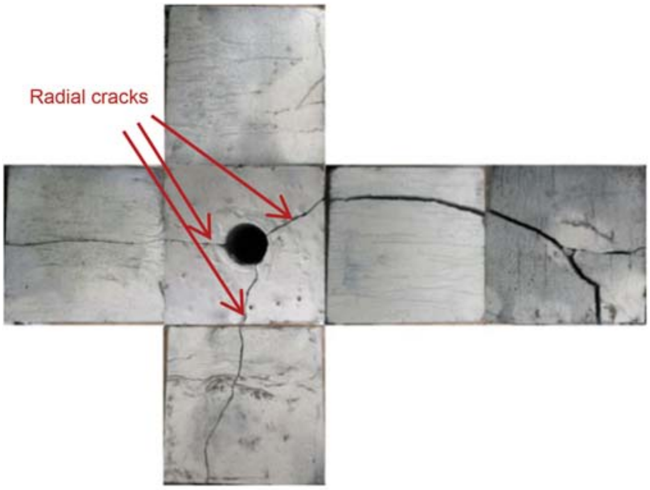

(a) Crack morphology of sample A

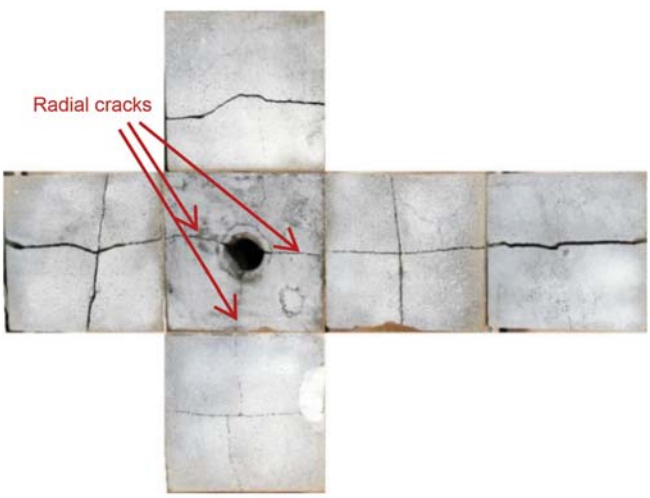

(b) Crack morphology of sample B

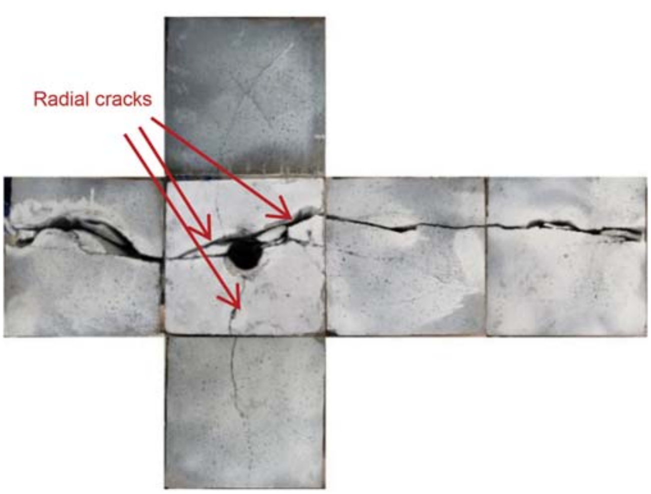

(c) Crack morphology of sample C

Fig. 7. Crack morphology of sample. (**a**) Crack morphology of sample A; (**b**) Crack morphology of sample B; (**c**) Crack morphology of sample C.

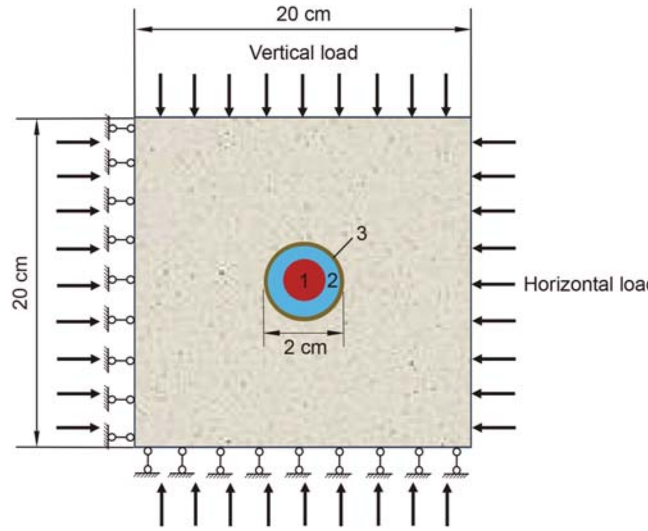

Fig. 8. Numerical simulation of the geometric model.

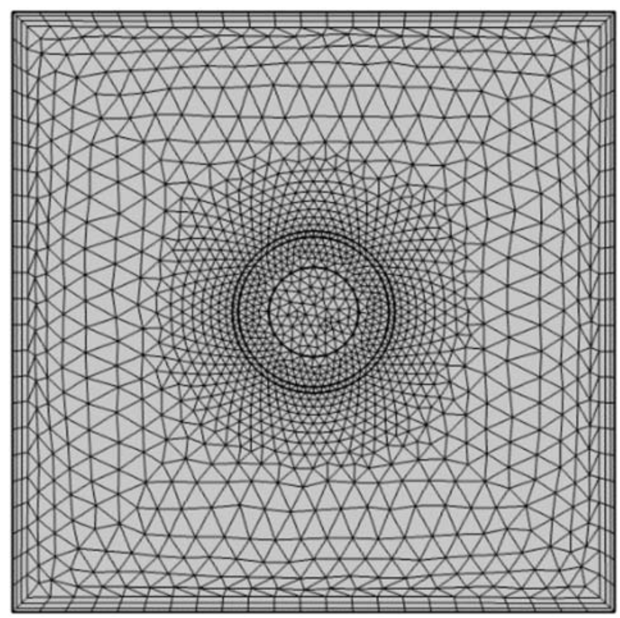

Fig. 9. Diagram of grid division.

$$\boldsymbol{\varepsilon_{ij}} = \frac{1}{2}\left(\boldsymbol{u_{i,j}} + \boldsymbol{u_{j,i}}\right) \tag{2}$$

$$\boldsymbol{\sigma_{ij}} = \lambda \boldsymbol{\delta_{ij}} \boldsymbol{\varepsilon_{V}} + 2G\boldsymbol{\varepsilon_{ij}} \tag{3}$$

where λ and G are expressed as

$$\lambda = \frac{E\nu}{(1+\nu)(1-2\nu)}$$

$$G = \frac{E}{2(1+\nu)} \tag{4}$$

where $\boldsymbol{\sigma_{ij}}$ and $\boldsymbol{\varepsilon_{ij}}$ are total stress and total strain, $\boldsymbol{\sigma_{ij,j}}$ is the stress tensor component in the j direction, $\boldsymbol{\varepsilon_V}$ is the volume strain, $\boldsymbol{\varepsilon_V} = \boldsymbol{\varepsilon_{11}} + \boldsymbol{\varepsilon_{22}} + \boldsymbol{\varepsilon_{33}}$, $\boldsymbol{F_i}$ is volume force, ρ_s is rock density, $\boldsymbol{x}$ is rock

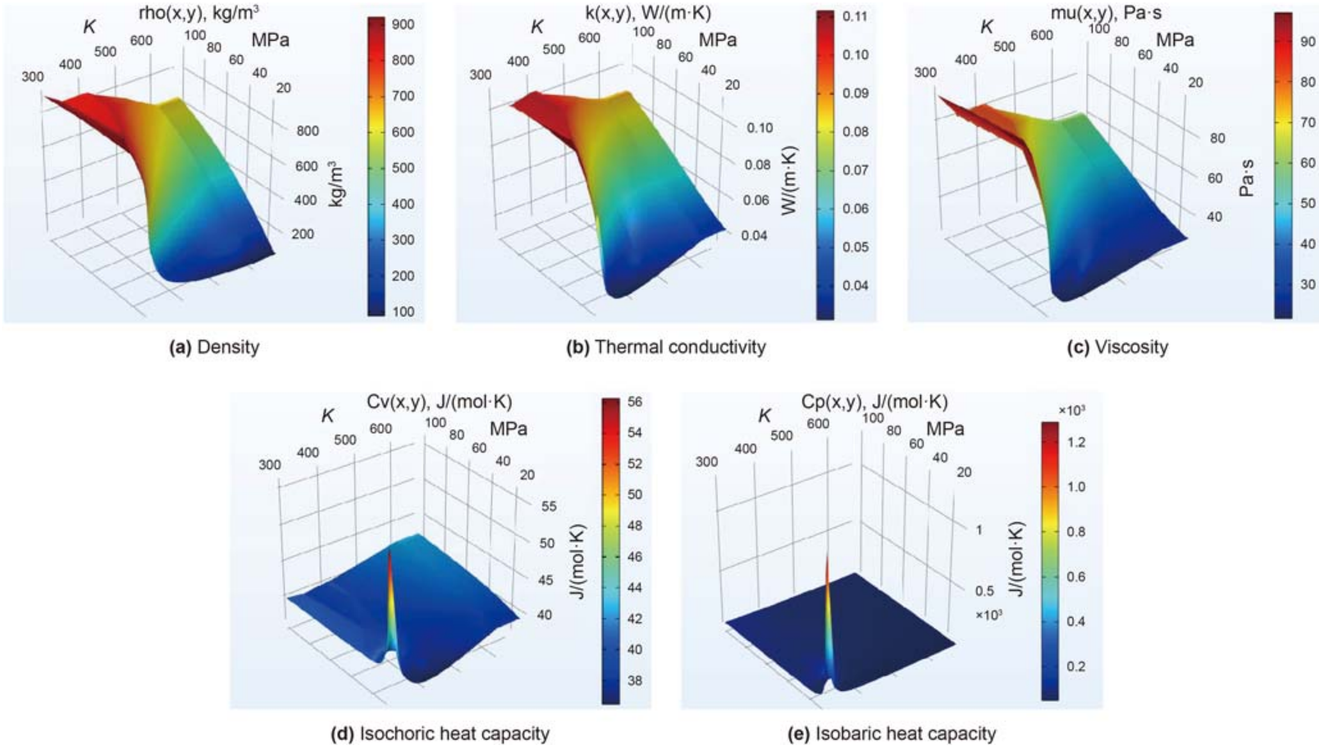

Fig. 10. Physical properties of CO_2 at different temperatures and pressures.

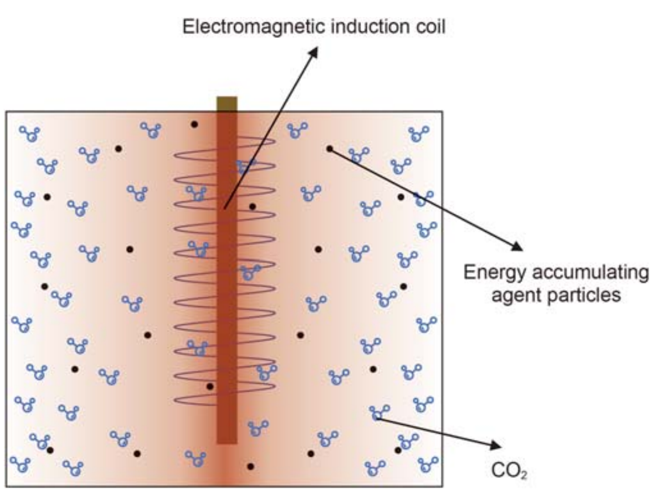

Fig. 11. Schematic diagram of exothermic process of energy accumulating agent.

displacement, $\boldsymbol{u_{i,j}}$ and $\boldsymbol{u_{j,i}}$ are displacement components, $\boldsymbol{\delta_{ij}}$ is Kronecker constant, G is shear modulus, λ is Lame coefficient, E is elastic modulus, and ν is Poisson's ratio.

(2) Rock damage evolution equation

When the stress state of rock mesoscopic unit satisfied the theory of maximum normal stress intensity, the element began to accumulate damage and finally broke down (Li et al., 2017). The elastic modulus of rock decreased gradually with the accumulation of damage, which could be expressed as (Rayudu et al., 2019; Li et al., 2017)

$$E = (1-d)E_0 \tag{5}$$

where E, E_0 are the elastic modulus of damaged and undamaged rock elements respectively, and d is the damage variable. $d = 0$ represents the undamaged state of rock, $0 < d < 1$ corresponds to different degrees of damage in the rock, and $d = 1$ represents the complete damage state of rock.

The elastic brittle damage model was adopted for rock. When subjected to uniaxial tension, the damage evolution equation of rock mesoscopic unit could be expressed as (Li et al., 2017)

$$d = \begin{cases} 0, \ \boldsymbol{\varepsilon} < \boldsymbol{\varepsilon_{to}} \\ 1 - \dfrac{\lambda \boldsymbol{\varepsilon_{to}}}{\boldsymbol{\varepsilon}}, \ \boldsymbol{\varepsilon_{to}} \le \boldsymbol{\varepsilon} < \boldsymbol{\varepsilon_{tu}} \\ 1, \ \boldsymbol{\varepsilon} \ge \boldsymbol{\varepsilon_{tu}} \end{cases} \tag{6}$$

where λ is the residual tensile strength coefficient, $\boldsymbol{\varepsilon}_{to}$ is the tensile strain corresponding to the elastic limit, ultimate tensile strain $\varepsilon_{tu} = \eta \cdot \varepsilon_{to}$, and η is the ultimate strain coefficient.

Rock is a kind of strain-softening material. When rock reaches its failure criterion and enters the failure zone, it undergoes strain softening and shows the characteristics of strength degradation, modulus reduction and volume expansion. These characteristics are more obvious under high temperature and high pressure, so the strain softening characteristics of the rock mass must be considered in analyses of thermal fracturing. In the bottom parameters of the numerical model, the residual tensile strength coefficient λ is determined by using the exponential strain softening relationship, and the expression is as follows.

$$\lambda = \exp^{-\frac{\varepsilon_q - \varepsilon_{to}}{\varepsilon_f - \varepsilon_{to}}} \tag{7}$$

$$\boldsymbol{\varepsilon}_{\mathrm{f}}=\frac{G_{\mathrm{f}}}{h_{\mathrm{cb}}\boldsymbol{\sigma}_{\mathrm{p}}}+\frac{1}{2}\boldsymbol{\varepsilon}_{to} \quad (8)$$

where $\boldsymbol{\varepsilon}_{\mathrm{q}}$ is the equivalent strain, $\boldsymbol{\varepsilon}_{\mathrm{f}}$ is the strain softening parameter, G_{f} is the fracture energy of material, h_{cb} is the damage characteristic size, and $\boldsymbol{\sigma}_{\mathrm{p}}$ is the tensile strength.

(3) Convection diffusion equation and combustion rate

CO_2 energy accumulating miscible fluid is a mixture of Sc-CO_2 and energy accumulating agent particles. According to the calculation method for physical parameters proposed by Yang et al. (2020), the reasonable parameters of CO_2 energy accumulating miscible fluid were reasonably modified. In the initial state, its concentration distribution is not uniform. Therefore, energy accumulating agent particles will diffuse from the high concentration area to the low concentration area while burning and generating a lot of heat. The CO_2 in the cracking tube is also moving continuously. This process needs to consider the combined effects of convection and diffusion:

The convection diffusion equation between energy accumulating agent particles and CO_2 is

$$J=-D'\nabla c+c\boldsymbol{V} \quad (9)$$

$$\partial c/\partial t+\nabla\bullet J=R' \quad (10)$$

where ∇ is Laplace operator, J is the diffusion flux, c is the fluid concentration, D' is the diffusion coefficient of energy accumulating agent particles, $\boldsymbol{V}$ is the velocity of fluid, and R' is the combustion rate of energy accumulating agent particles.

It was assumed that time t_0 was required for the combustion of all the energy accumulating agent particles in CO_2 energy accumulating miscible fluid. According to the experimental results, it could be assumed that there was an exponential relationship between the combustion rate and the concentration of the energy accumulating agent particles (Eq. (11)). The concentration and reaction rate also satisfied Eq. (12). After integration and derivation, the formula of combustion rate of energy accumulating agent particles (Eq. (13)) was deduced.

$$R'=c\cdot\exp^{-\frac{t}{t_0}} \quad (11)$$

$$c=c_0-\int_0^t R'\mathrm{d}t \quad (12)$$

$$R'=c_0\cdot\exp^{-t_0-\frac{t}{t_0}+t_0e^{-\frac{t}{t_0}}} \quad (13)$$

where c_0 is the initial concentration of energy accumulating agent particles, t is the combustion time of energy accumulating agent particles, and t_0 is the time required for all energy accumulating agent particles to burn.

(4) Governing equation of flow field

The Navier-Stokes equation is suitable for the real fluid in macroscopic motion. The Navier-Stokes equation can be used to describe the turbulent motion of CO_2 in the cracking tube and the nonlinear flow of fracturing fluid in the fracture.

There is rapid seepage in the rock formation near the borehole driven by fluid velocity, pressure and gravity. The dissipation of shear energy can't be ignored. Brinkman equation is suitable for describing the rapid seepage process in saturated porous media and can calculate the kinetic energy dissipation caused by viscous shear force (Hwang and Advani, 2010). Therefore, Brinkman equation is used to describe the fluid flow in the fractured and porous areas of rock formation near the borehole.

The governing equation of CO_2 free flow process in cracking tube can be expressed by Navier-Stokes equation.

$$\underbrace{\rho(\partial\boldsymbol{V}/\partial t+\boldsymbol{V}\cdot\nabla\boldsymbol{V})}_{1}=\underbrace{-\nabla\boldsymbol{p}}_{2}+\underbrace{\nabla\cdot\left(\mu\left(\nabla\boldsymbol{V}+(\nabla\boldsymbol{V})^{\boldsymbol{T}}\right)-\frac{2}{3}\mu(\nabla\cdot\boldsymbol{V})\boldsymbol{I}\right)}_{3}+\underbrace{\boldsymbol{F}+\rho\boldsymbol{g}}_{4} \quad (14)$$

where each item corresponds to inertial force (1), pressure (2), viscous force (3) and external force (4) acting on the fluid respectively, ρ is the fluid density, $\rho\boldsymbol{g}$ is the gravity term, $\boldsymbol{V}$ is the fluid velocity, $\boldsymbol{p}$ is the fluid pressure, μ is the hydrodynamic viscosity, and $\boldsymbol{I}$ is the identity matrix.

The model utilized the Brinkman equation to simulate fluid flow in rock fractures and pore areas. The Brinkman equation is expressed as

$$\frac{\rho}{\phi}\left(\partial\boldsymbol{V}\Big/\partial t+(\boldsymbol{V}\cdot\nabla)\frac{\boldsymbol{V}}{\phi}\right)=\nabla(-\boldsymbol{pI}+\tau)-\left(\frac{\mu}{k}+\beta\rho|\boldsymbol{V}|+\frac{Q_{\mathrm{m}}}{\phi^2}\right)\boldsymbol{V}+\boldsymbol{F}+\rho\boldsymbol{g} \quad (15)$$

where ϕ is the porosity, k is the permeability, β is the isothermal compressibility, and Q_{m} is the source term.

A semi-empirical formula was proposed based on the observed results of porosity changing with damage in fracturing experiments.

$$\phi=\phi_0\cdot\exp^{\frac{\xi d}{3}} \quad (16)$$

where ξ is the influence coefficient of damage on porosity.

The relationship between permeability and porosity satisfied the following formula (Pillai et al., 2018; Zhu et al., 2013).

$$k\Big/k_0=(\phi/\phi_0)^3 \quad (17)$$

where k_0 and ϕ_0 are the permeability and porosity of the rock in the initial state respectively, and k is the permeability corresponding to the ϕ state.

Through Eqs. (16) and (17), the relationship between permeability and damage is as follows.

$$k=k_0\cdot\exp^{\xi d} \quad (18)$$

(5) Temperature field governing equation

The temperature and flow fields are coupled by non-isothermal flow, and the energy conservation equation of fluid and rock can be expressed as

$$\rho C_p \frac{\partial T}{\partial t} + \rho C_p \boldsymbol{V} \cdot \nabla T = \nabla \cdot (K \nabla T) + \tau : \nabla \boldsymbol{V} + \left(\frac{\partial \boldsymbol{p}}{\partial t} + \boldsymbol{V} \cdot \nabla \boldsymbol{p} \right) + Q \tag{19}$$

where K is the thermal conductivity, C_p is the isobaric heat capacity, Q is the heat source power, T is the temperature, and $\boldsymbol{p}$ is the fluid pressure.

The mass fraction of energy accumulating agent particles decreases as they burnt, and the mass fraction is proportional to the heat source power. It is preliminarily assumed that the heat source power Q is

$$Q = Q_0 \cdot W \tag{20}$$

where Q_0 is the initial value of heat source power; W is the mass fraction of the energy accumulating agent, that is, the percentage of the mass of energy accumulating agent particles to the total mass of the fluid mixture.

(6) Multi-physical field coupling medium

A multi-field coupled numerical model of Sc-CO_2 thermal fracturing was established by using the solid and fluid heat transfer, free and porous medium flow, solid mechanics and convection diffusion modules in COMSOL Multiphysics software. The relevant coupling process is shown in Fig. 12.

In the basic governing equations of multi-field coupling, the damage variable also affects the permeability and porosity equations of rock because the damage variable is related to the strain of rock. Therefore, in the governing equations of rock stress field (Eq. (3)) and seepage field (Eq. (15)), the strain of rock $\boldsymbol{\varepsilon}$ is a coupling term.

The governing equations of rock stress field (Eq. (3)) and damage field (Eqs. (5) and (6)) are coupled by elastic modulus E and strain $\boldsymbol{\varepsilon}$.

The governing equations of temperature field (Eq. (19)), seepage field (Eq. (15)) and free flow process (Eq. (14)) are coupled by the density ρ and velocity $\boldsymbol{V}$ of fluid.

The rock permeability equation (Eq. (18)) and the porosity equation (Eq. (16)) are coupled by damage variable d.

3.4. Verification of numerical simulation method

According to the Sc-CO_2 thermal fracturing experimental results

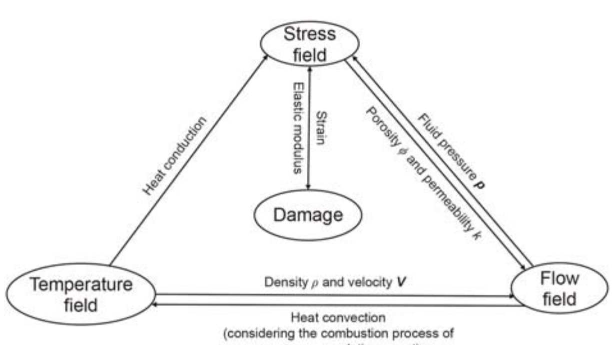

Fig. 12. Schematic diagram of multi-field coupling process.

of sample A in Section 2, the same material parameters were used in the multi-field coupled numerical model. The multi-field coupled numerical model adopted 8 MPa vertical confining pressure and 6 MPa horizontal confining pressure, the initial pressure of CO_2 was 15 MPa and the dosage of energy accumulating agent was 15 g.

It can be seen from Fig. 13 that the direction and number of cracks in the numerical simulation results of Sc-CO_2 thermal fracturing were basically consistent with the experimental results of sample A, and the time spent in the cracking process was basically consistent. This showed that the multi-field coupled numerical model had high accuracy and could basically simulate the number and propagation direction of cracks.

4. Analysis of numerical model results

4.1. Setting of numerical experiment simulation group

Due to the limitations of experimental conditions, the triaxial pressures of high-strength cement specimens in the experiment were 5, 6, and 8 MPa, respectively. The pressure values were small, and were different from the confining pressure of deep rocks. However, larger confining pressure could be used to simulate the deep crustal environment in numerical simulation. This study regarded the burial depth of 600 m as the critical depth for deep engineering. As shown in Table 3, the rock mechanical parameters in the numerical model were based on the mechanical parameters of dense sandstone buried at depths of 600–700 m.

Energy density refers to the energy contained in a unit volume of a material. In COMSOL Multiphysics, energy density couldn't be directly used as an independent variable to study its effect on the Sc-CO_2 thermal fracturing process. However, when the temperature and container volume were constant, the initial pressure of CO_2 determined the total amount and density of the fluid. The power of the heat source represented the heat release rate of the energy accumulating agent, which affected the amount of energy released over a period of time. Therefore, the influence of energy density could be studied indirectly by changing the initial CO_2 pressure and heat source power.

In the numerical simulation, the vertical load and horizontal load of rock were set as 15 MPa. The specific numerical experimental scheme was shown in Table 4.

4.2. Analysis of dynamic evolution process of rock damage

This model defined damage variables based on the reduction of rock mass elastic modulus and the strain of mesoscopic unit. The reduction of elastic modulus could quantify the macroscopic mechanical effect of internal damage in rock mass, namely the process of crack initiation, expansion and penetration. In the numerical model, when the damage degree of rock mesoscopic unit was greater than 0.9, it approached the failure state.

Taking the A3 simulation group as an example, according to the ideal gas equation PV = nRT, when the volume of the cracking tube remained unchanged, the pressure of the fluid increased when the temperature rose and decreased when the temperature dropped. Therefore, the changes in fluid pressure and temperature curves before point D in Fig. 14 were basically consistent.

To better describe CO_2 pressure during the whole fracturing process, the CO_2 pressure curve in Fig. 14 was divided into the initial rising section AB, convective diffusion section BC, stable rising section CD, fluctuating rising section DE, and pressure dropping section EG.

In section AB, the energy accumulating agent particles began to burn and emit a large amount of heat, and the fluid pressure also

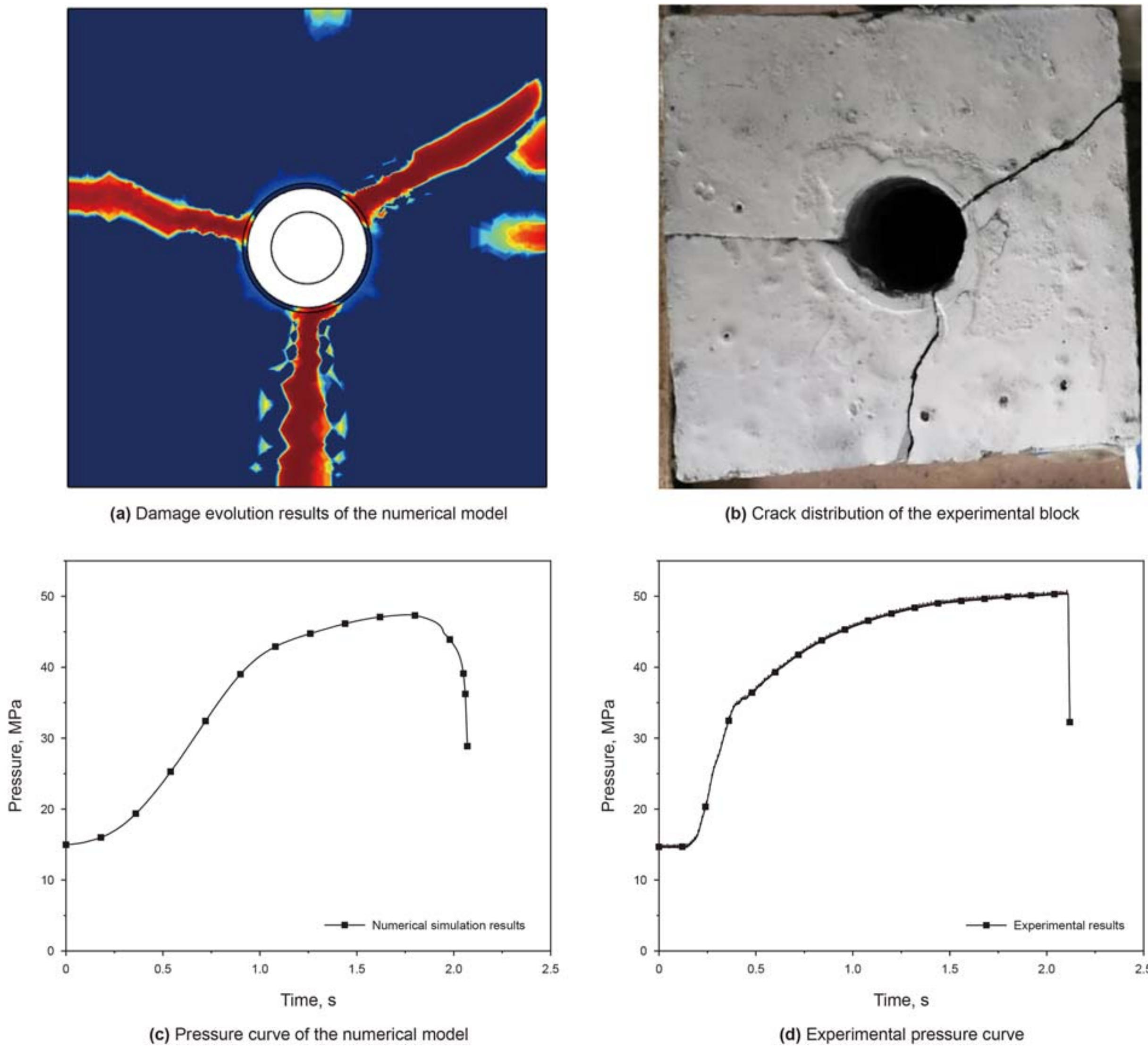

Fig. 13. Comparison between numerical simulation results and experimental results. **(a)** Damage evolution results of the numerical model; **(b)** Crack distribution of the experimental block; **(c)** Pressure curve of the numerical model; **(d)** Experimental pressure.

Table 3
Mechanical parameters of rock.

Density, $kg \cdot m^{-3}$	Elastic modulus, GPa	Poisson's ratio	Tensile strength, MPa	Uniaxial compressive strength, MPa	Permeability, m^2	Porosity
2500	25	0.13	10.1	106	4.5×10^{-17}	0.06

Table 4
Numerical experimental scheme of Sc-CO_2 thermal fracturing.

Simulation group	Initial value of heat source power, $W \cdot m^{-3}$	CO_2 initial pressure, MPa
A1	2×10^8	10
A2	3×10^8	10
A3	4×10^8	10
A4	5×10^8	10
A5	6×10^8	10
B1	5×10^8	8
B2	5×10^8	9
B3	5×10^8	10
B4	5×10^8	12

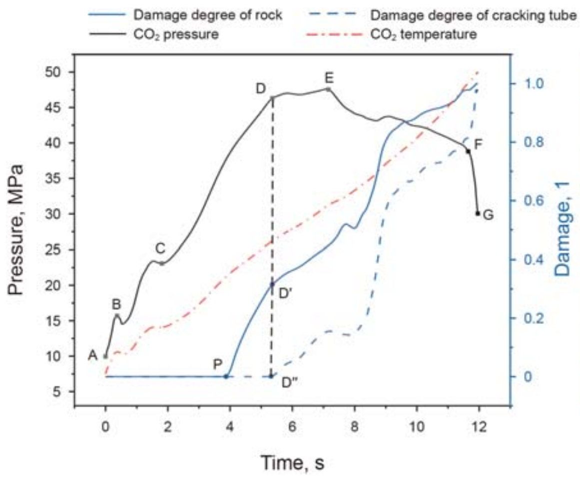

Fig. 14. Pressure-damage degree-temperature diagram of the A3 simulation group.

rose. At this time, CO_2 was in a state of coexistence of gas and liquid.

In the convection diffusion stage (section BC), the time was in the approximate range from 0.28 to 2 s. As shown in Fig. 15, the energy accumulating agent particles and the CO_2 at lower ambient temperature began to convection and diffusion, thus the temperature began to enter a stable transition period. Point B ($t = 0.28$ s) in the curve was the starting point of the CO_2 phase transition, which absorbed a large amount of heat. Therefore, the fluid temperature and pressure curve decreased rapidly after point B.

In section CD, the pressure rose steadily. At this stage, the energy accumulating agent particles were fully mixed with CO_2, and the energy accumulating agent particles continued to emit heat, so the temperature and pressure of CO_2 began to rise steadily.

In the PD' section, the damage degree of the rock rose rapidly, but the corresponding damage degree of the cracking tube was 0. This was because the cracking tube was prone to expansion and deformation. The rock would exert pressure to limit the deformation of the cracking tube, and the rock would be subjected to the reaction force exerted by the cracking tube, causing the rock to be damaged before the cracking tube. This segment corresponded to step 1 and step 2 in Fig. 16.

In section DE, the CO_2 pressure was in the fluctuation rising stage, and point E corresponded to the peak pressure of CO_2. Point D ($t = 5.35$ s) corresponded to the initial damage point D'' of the cracking tube, and the CO_2 pressure just reached the fracturing pressure of the cracking tube. As shown in step 3 of Fig. 16, the cracking tube began to damage at this time. Due to the constraints of concrete and the external boundary of concrete, a large counterforce was generated, resulting in the peak pressure of Sc-CO_2 exceeding the yield strength of the cracking tube.

In section EG, the CO_2 pressure was decreasing, and the rock damage showed a fluctuating upward trend. The cracks began to form and gradually weakened the strength of rock. Point G ($t = 11.95$ s) corresponded to step 6 of Fig. 16, at which the degree of rock fracture damage was large. The loss of a large amount of fracturing fluid caused the CO_2 pressure to drop precipitously in the FG section.

4.3. Influence of heat source power on thermal shock cracking process

In CO_2 energy accumulating miscible fluid, the liquid CO_2 absorbed the heat released by the combustion of the energy accumulating agent particles and converted the chemical energy into its own heat energy. The greater the power of the heat source, the greater the amount of heat released per unit time. Therefore, it

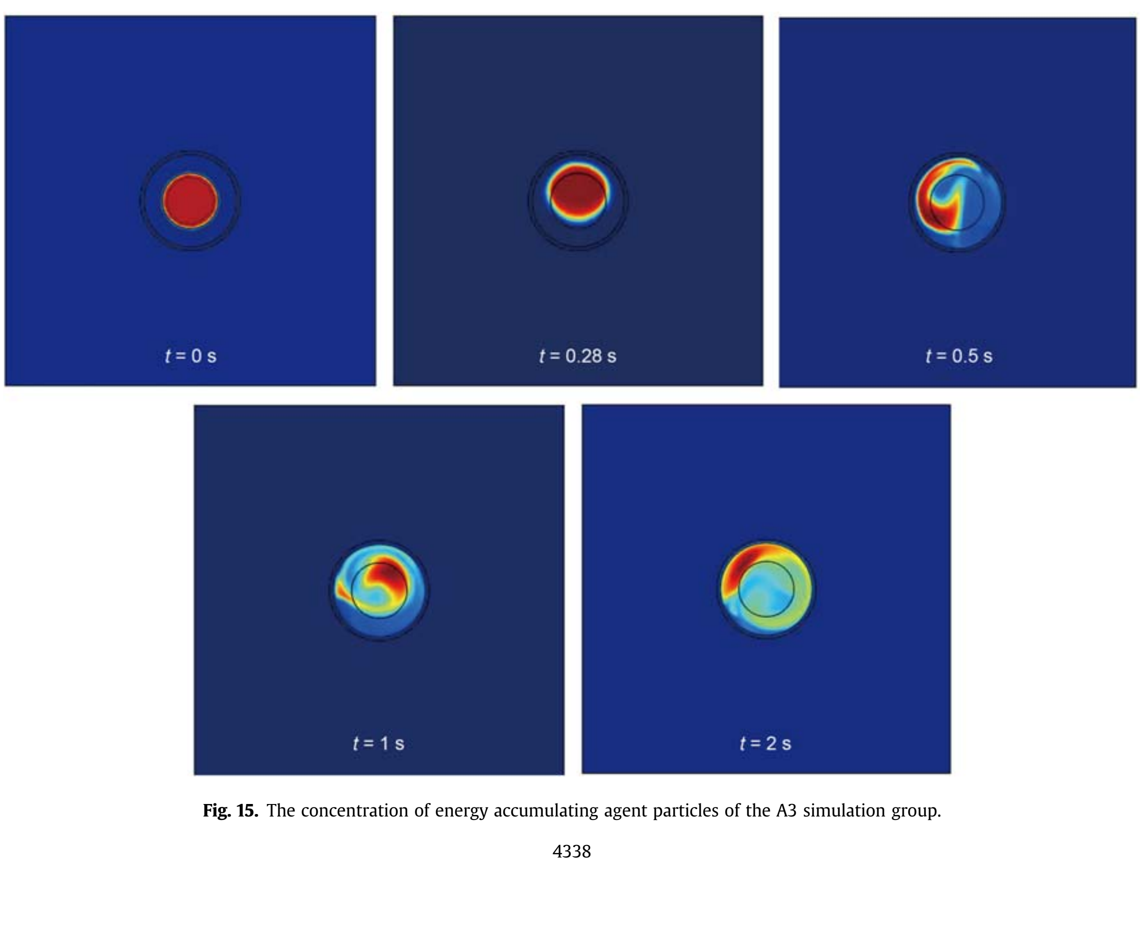

Fig. 15. The concentration of energy accumulating agent particles of the A3 simulation group.

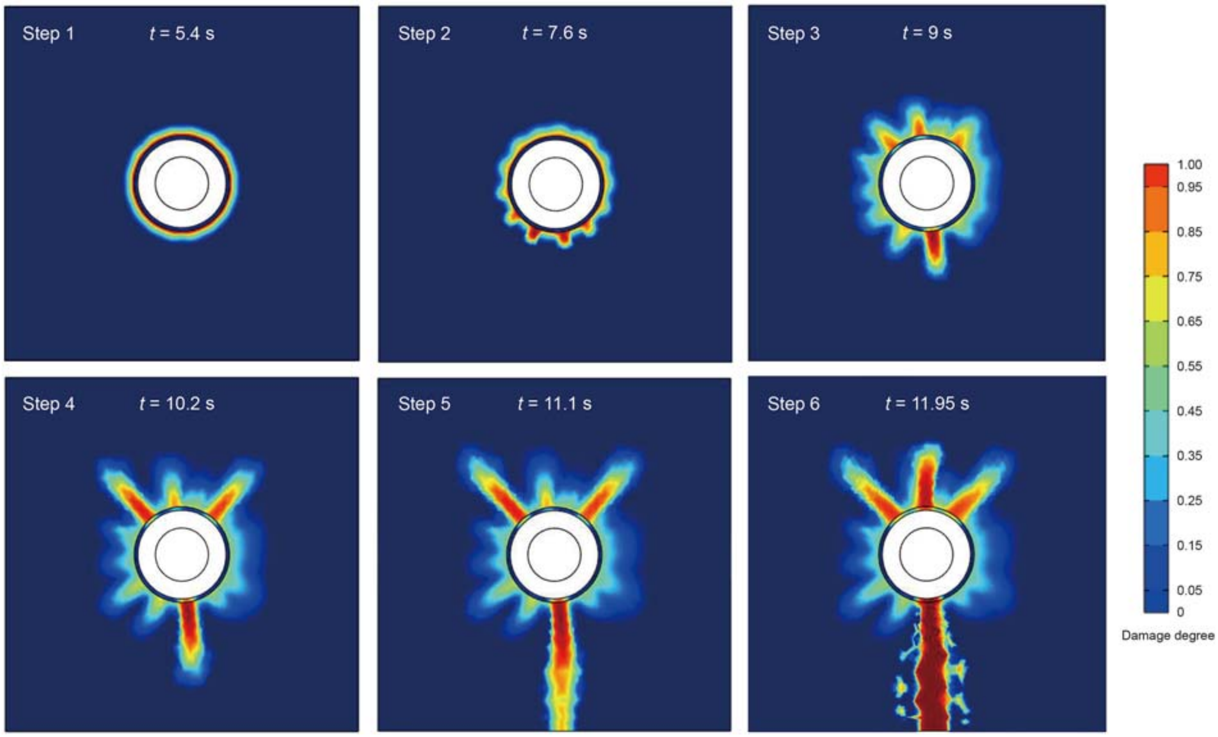

Fig. 16. Damage evolution of the A3 simulation group.

Table 5
Parameters of key points in the numerical simulation.

Simulation group	Peak pressure, MPa	Time at the starting point of CO_2 phase transition, s	CO_2 complete phase transition time point, s	Fracture initiation pressure of the cracking tube, MPa	Fracture initiation time of the cracking tube, s
A1	43.02	2.17	4.69	42.68	16.43
A2	47.25	0.43	1.10	46.38	6.53
A3	47.73	0.28	0.95	46.49	5.39
A4	49.76	0.22	0.75	46.92	3.24
A5	53.15	0.18	0.43	47.81	1.21

was easier to achieve the energy necessary for initiation cracks.

As shown in Table 5, with the increase of heat source power, the time at the starting point of CO_2 phase transition and the time required to complete the phase transformation both decreased correspondingly. When the initial value of the heat source power was from 2×10^8 to 6×10^8 W/m^3, the fracture initiation pressure increased from 42.68 to 47.81 MPa, an increase of 11.29%, and the fracture initiation time decreased from 16.43 to 1.21 s, a decrease of 92.64%.

As shown in Table 5 and Fig. 17, the peak pressure, fracture initiation pressure and initiation time of the A1 simulation group were quite different from those of the other simulation groups, and the crack length was short. It could be inferred that the amount of energy accumulating agent was insufficient at this time.

Changing the heat source power was essentially changing the severity of CO_2 phase transition. As shown in Figs. 18 and 19, the overall rising rate of temperature curve and pressure curve increased with the increase of heat source power. Meanwhile, the time required for the CO_2 to reach peak pressure became shorter and shorter. It could be seen from Fig. 20 that the fracture initiation time of rock was advanced and the total time required for the rock damage degree to reach “1” became shorter with the increase of heat source power.

On the whole, properly increasing the heat source power can make CO_2 enter the supercritical state faster, improve the heating and pressurization rate of Sc-CO_2, accelerate the damage degree of rock, and shorten the whole fracturing cycle time.

4.4. Influence of initial pressure of CO_2 on thermal shock cracking process

The process simulated in this study was a closed one-time thermal fracturing, which initially made the liquid CO_2 inside the cracking tube reach the set initial pressure, keeping the inlet and outlet of the cracking tube closed without the injection of external CO_2. Therefore, when the temperature and container volume were constant, the initial pressure of CO_2 determined the total amount and density of CO_2.

The temperature and pressure of CO_2 would rapidly increase with the combustion and heat release of the energy accumulating agent particles. By comparing and analyzing the B1, B2, B3, and B4 simulation groups, it could be seen that the fracture initiation time of the cracking tube was greater than the time point when all CO_2 entered the supercritical state (see Table 6). All CO_2 entered the supercritical state could effectively avoid energy loss.

As the initial pressure of CO_2 increased, the pressure values of all

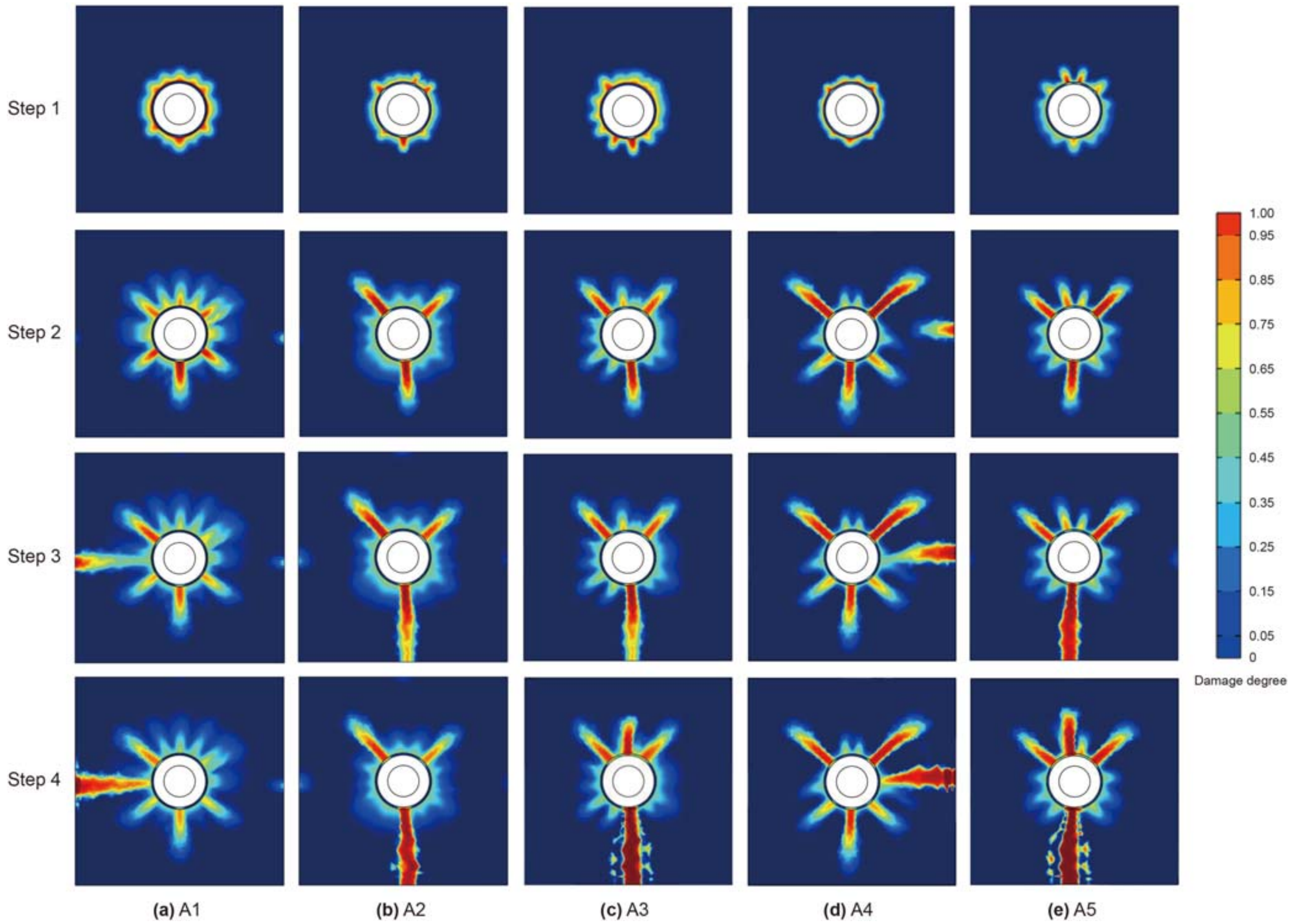

Fig. 17. Rock damage areas under different heat source powers.

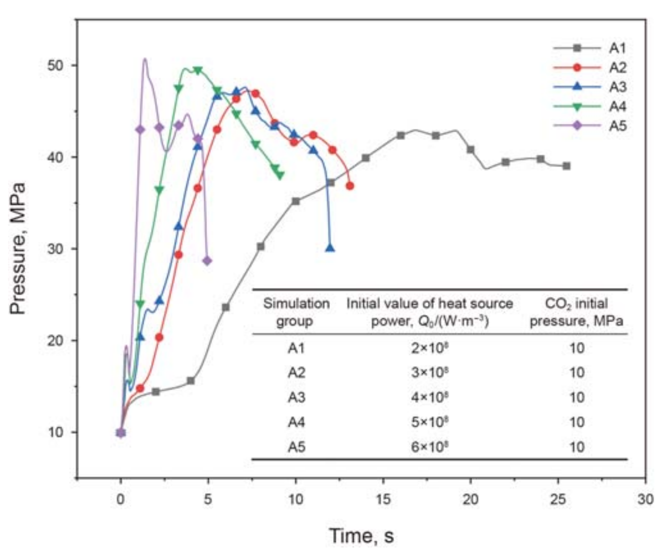

Fig. 18. Average pressure curve of CO_2.

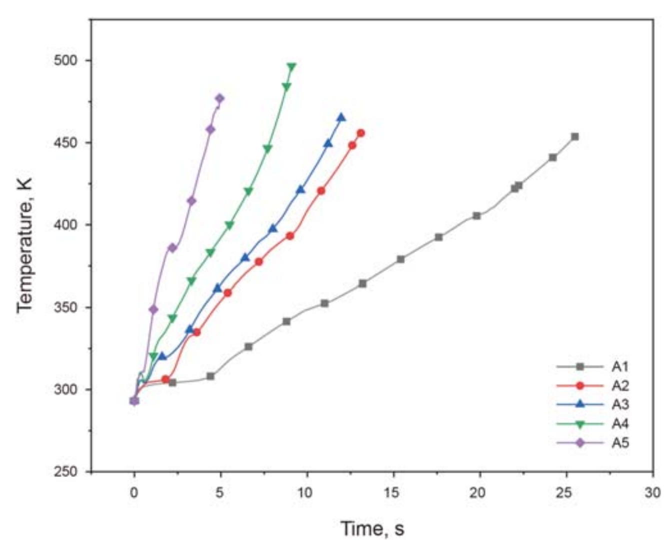

Fig. 19. Average temperature curve of CO_2.

CO_2 complete phase transition nodes in the cracking tube increased, and the fracture initiation time of the cracking tube also increased. The starting time of CO_2 phase transition and the peak pressure of CO_2 remained fluctuating at around 0.24 s and 50 MPa, respectively (see Table 6). The experimental results in section 2.3 indicated that increasing the initial pressure of CO_2 had little effect on the peak pressure of the fluid, and the experimental results maintained good consistency with the numerical simulation

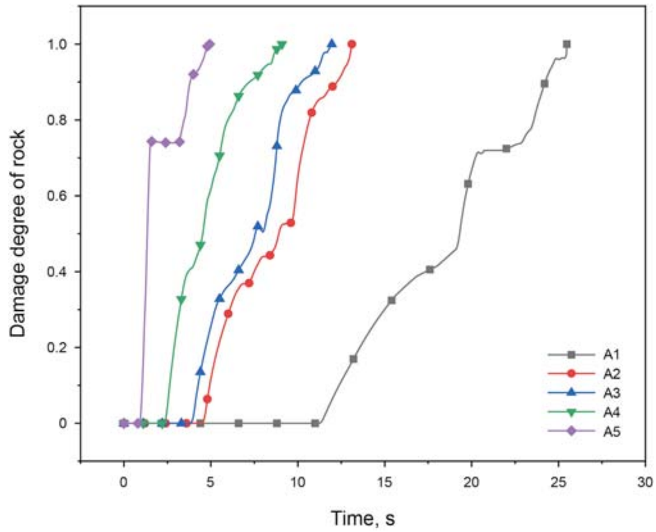

Fig. 20. Damage degree curve of rock.

results. This indirectly proved the accuracy of the multi-field coupling numerical model of Sc-CO_2 thermal fracturing.

As shown in Fig. 21, the distribution of cracks was random, and the direction of the through cracks wasn't fixed. It could be seen from Figs. 22 and 23 that the temperature and pressure curves were basically consistent before CO_2 phase transition. After CO_2 phase transition, the final temperature of CO_2 and the rising rate of the average temperature curve of CO_2 decreased with the increase of CO_2 initial pressure. The final temperature value that could be reached was 484.27 K when the initial pressure of CO_2 in the cracking tube was 8 MPa. The final temperature value that could be reached was only 446.50 K when the initial pressure of CO_2 increased to 12 MPa. It could be reasonably inferred that the increase of CO_2 initial pressure meant the increase of CO_2 total amount when the initial value of heat source power remained constant. Heating more fluid with the same heat source would naturally reduce the maximum temperature that the fluid could ultimately reach.

Under the condition of maintaining constant heat source power,

Table 6
Parameters of key points in the numerical simulation.

Simulation group	Peak pressure, MPa	Time at the starting point of CO_2 phase transition, s	CO_2 complete phase transition time point, s	Complete phase transition node pressure, MPa	Fracture initiation time of the cracking tube, s
B1	50.78	0.25	0.46	14.92	2.47
B2	51.21	0.24	0.47	15.67	3.15
B3	49.76	0.22	0.75	16.65	3.24
B4	48.98	0.25	0.42	16.98	3.46

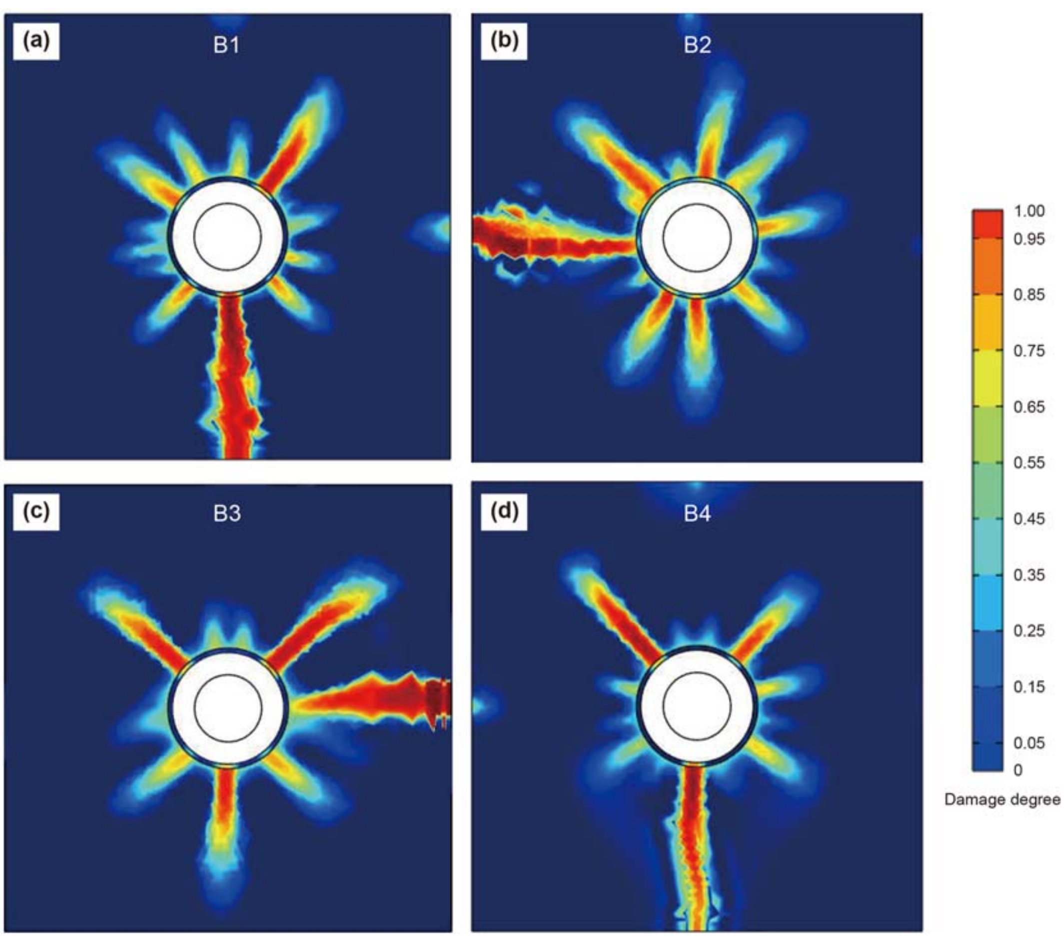

Fig. 21. Rock damage areas under different initial CO_2 pressures.

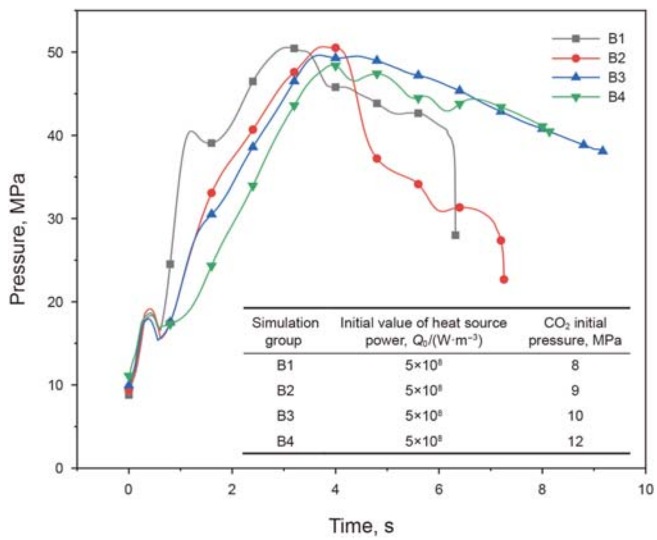

Fig. 22. Average pressure curve of CO_2.

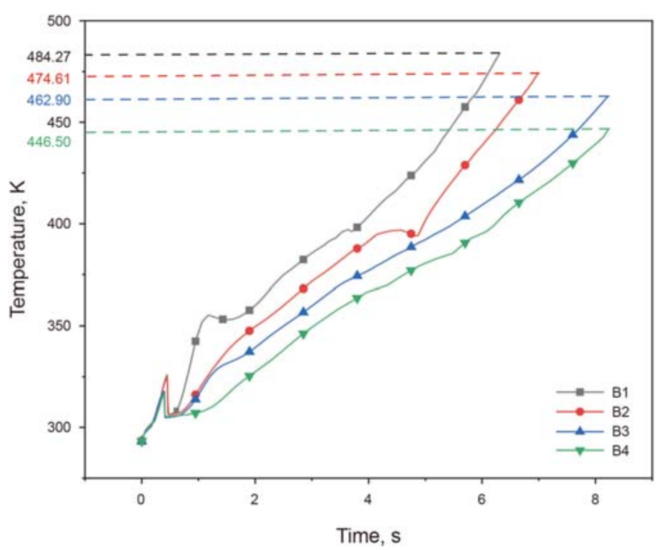

Fig. 23. Average temperature curve of CO_2.

the growth rate of CO_2 pressure in four experiments was introduced as a reference, which was the formula $p' = \Delta P/\ t$. In the formula, ΔP was the difference between the peak pressure and the initial pressure of fluid, and t was the time required to reach the peak pressure. The growth rates of the four experiments were 14.28, 10.61, 10.17, and 9.27, respectively. This indicated that the growth rate of pressure during the fracturing process gradually decreased with the CO_2 initial pressure increased. This was also caused by the increase in the total amount of CO_2 when the heat source power remained constant.

Overall, as the CO_2 initial pressure increases, the maximum temperature and the growth rate of CO_2 pressure during the cracking process will decrease accordingly, but the peak pressure of CO_2 doesn't change much.

5. Conclusion

On the basis of laboratory experiment and multi-field coupling control equations, a numerical model of Sc-CO_2 thermal fracturing was established by using COMSOL Multiphysics software. Relevant studies were carried out around the rock damage evolution process, the characteristics of CO_2 pressure curve and the influence factors of thermal shock cracking process. The main conclusions were as follows:

The energy accumulating agent was a new type of porous high energy accumulating alloy heating material, which provided energy for the Sc-CO_2 thermal fracturing process. According to the experimental results, the combustion rate formula of energy accumulating agent was deduced in this paper. Meanwhile, the heat source power expression was established based on the proportional relationship between the mass fraction of energy accumulating agent particles and the heat source power.

The numerical simulation results indicated that the maximum temperature of CO_2 and the growth rate of CO_2 pressure during the fracturing process would decrease accordingly with the increase of CO_2 initial pressure. But the change of CO_2 peak pressure wasn't significant. Appropriately increasing the heat source power could improve the Sc-CO_2 thermal fracturing effect, make CO_2 enter the supercritical state faster, increase the number of fractures and the peak pressure of CO_2, and shorten the whole fracturing cycle time.

Data availability

Fluid parameters are from the https://webbook.nist.gov/chemistry/fluid/.

CRediT authorship contribution statement

Shao-Bin Hu: Writing – original draft, Resources, Methodology. **Lin Zhang:** Writing – review & editing, Writing – original draft, Software. **Yu-Kang Cai:** Writing – review & editing, Software. **Shuo-Gang Pang:** Investigation. **Zheng-Yong Yan:** Validation. **Qiang Zhang:** Funding acquisition.

Declaration of competing interest

We declare that we have no financial and personal relationships with other people or organizations that can inappropriately influence our work, there is no professional or other personal interest of any nature or kind in any product, service and/or company that could be construed as influencing the position presented in, or the review of, the manuscript entitled.

Acknowledgments

This work is financially supported by National Key R&D Program-Sino US intergovernmental Cooperation Project (No. 2023YFE0120500) , Science and Technology Program of the Ministry of Housing and Urban-Rural Development of the People's Republic of China (No. 2021-K-087), the Surface Project of the Natural Science Foundation of Jiangsu Province, China (No. BK20201313) and the State Key Laboratory Open Fund Project of China (No. HKLBEF202004).

References

Chen, H., Wang, Z., Qi, L., et al., 2017. Effect of liquid carbon dioxide phase change fracturing technology on gas drainage. Arabian J. Geosci. 10 (14), 314. https://doi.org/10.1007/s12517-017-3103-0.

Chen, H., Hu, Y., Kang, Y., et al., 2021. Advantages of supercritical CO_2 compound fracturing in shale on fracture geometry, complexity and width. J. Nat. Gas Sci. Eng. 93, 104033. https://doi.org/10.1016/j.jngse.2021.104033.

Cai, C., Kang, Y., Yang, Y., et al., 2020. Experimental investigation on flow field and induced strain response during SC-CO_2 jet fracturing. J. Petrol. Sci. Eng. 195, 107795. https://doi.org/10.1016/j.petrol.2020.107795.

Ha, S.J., Choo, J., Yun, T.S., 2018. Liquid CO_2 fracturing: effect of fluid permeation on

the breakdown pressure and cracking behavior. Rock Mech. Rock Eng. 51, 3407–3420. https://doi.org/10.1007/s00603-018-1542-x.
Hwang, W.R., Advani, S.G., 2010. Numerical simulations of Stokes-Brinkman equations for permeability prediction of dual scale fibrous porous media. Phys. Fluids 22 (11), 197. https://doi.org/10.1063/1.3484273.
He, J., Zhang, Y., Li, X., et al., 2019. Experimental investigation on the fractures induced by hydraulic fracturing using freshwater and supercritical CO_2 in shale under uniaxial stress. Rock Mech. Rock Eng. 52, 3585–3596. https://doi.org/10.1007/s00603-019-01820-w.
Hu, S., Li, X., Bai, B., 2016. Carbon dioxide based strong active energy concentrator and its preparation method and application. National Invention Patent, CN105884562A.
Hu, S., Pang, S., Yan, Z., 2019. A new dynamic fracturing method: deflagration fracturing technology with carbon dioxide. Int. J. Fract. 220 (8), 99–111. https://doi.org/10.1007/s10704-019-00403-8.
Ishida, T., Chen, Y., Bennour, Z., et al., 2016. Features of CO_2 fracturing deduced from acoustic emission and microscopy in laboratory experiments. J Geophys Res-Sol. 121 (11), 8080–8098. https://doi.org/10.1002/2016JB013365.
Jiao, F., 2019. Re-recognition of "unconventional" in unconventional oil and gas. Petrol. Explor. Dev. 46 (5), 847–855. https://doi.org/10.1016/S1876-3804(19)60244-2.
Kohshou, I.O., Barati, R., Yorro, M.C., et al., 2017. Erratum to: economic assessment and review of waterless fracturing technologies in shale resource development: a case study. J Earth Sci-China 28 (5), 1191. https://doi.org/10.1007/s12583-017-0783-z.
Li, X., Wang, J., Elsworth, D., 2017a. Stress redistribution and fracture propagation during restimulation of gas shale reservoirs. J. Pet. Sci. Eng. 154, 150–160. https://doi.org/10.1016/j.petrol.2017.04.027.
Liang, T., Zhou, F., Lu, J., et al., 2017. Evaluation of wettability alteration and IFT reduction on mitigating water blocking for low-permeability oil-wet rocks after hydraulic fracturing. Fuel 209, 650–660. https://doi.org/10.1016/j.fuel.2017.08.029.
Li, Z., Li, L., Bo, H., et al., 2017b. Numerical investigation on the propagation behavior of hydraulic fractures in shale reservoir based on the DIP technique. J. Pet. Sci. Eng. 154, 302–314. https://doi.org/10.1016/j.petrol.2017.04.034.
Liu, L., Zhu, W., Wei, C., et al., 2018. Microcrack-based geomechanical modeling of rock-gas interaction during supercritical CO_2 fracturing. J. Pet. Sci. Eng. 164, 91–102. https://doi.org/10.1016/j.petrol.2018.01.049.
Li, Q., Luo, D., Feng, G., et al., 2019a. Dynamic characteristics of liquid CO_2 phase change fracturing, using experimental technique. Geotech. Geol. Eng. 37, 3387–3398. https://doi.org/10.1007/s10706-019-00853-w.
Li, T., Li, L., Tang, C., et al., 2019b. A coupled hydraulic-mechanical-damage geotechnical model for simulation of fracture propagation in geological media during hydraulic fracturing. J. Pet. Sci. Eng. 173, 1390–1416. https://doi.org/10.1016/j.petrol.2018.10.104.
Li, M., Zhang, F., Zhuang, L., et al., 2020a. Micromechanical analysis of hydraulic fracturing in the toughness-dominated regime: implications to supercritical carbon dioxide fracturing. Comput. Geosci. 24, 1815–1831. https://doi.org/10.1007/s10596-019-09925-5.
Li, S., Zhang, S., Ma, X., et al., 2020b. Coupled physical-chemical effects of CO_2 on rock properties and breakdown during intermittent CO_2-Hybrid fracturing. Rock Mech. Rock Eng. 53, 1665–1683. https://doi.org/10.1007/s00603-019-02000-6.
Liu, B., Suzuki, A., Ito, T., 2020. Numerical analysis of different fracturing mechanisms between supercritical CO_2 and water-based fracturing fluids. Int J Rock Mech Min 132, 104385. https://doi.org/10.1016/j.ijrmms.2020.104385.
Li, N., Wang, C., Zhang, S., et al., 2021. Recent advances in waterless fracturing technology for the petroleum industry: an overview. J. Nat. Gas Sci. Eng. 92 (1), 103999. https://doi.org/10.1016/j.jngse.2021.103999.
Middleton, R., Viswanathan, H., Currier, R., et al., 2014. CO_2 as a fracturing fluid: potential for commercial-scale shale gas production and CO_2 sequestration. Energy Proc. 63, 7780–7784. https://doi.org/10.1016/j.egypro.2014.11.812.
Middleton, R.S., Carey, J.W., Currier, R.P., et al., 2015. Shale gas and non-aqueous fracturing fluids: opportunities and challenges for supercritical CO_2. Appl. Energy 147, 500–509. https://doi.org/10.1016/j.apenergy.2015.03.023.
Meng, M., Qiu, Z., 2018. Experiment study of mechanical properties and microstructures of bituminous coals influenced by supercritical carbon dioxide. Fuel 219, 223–238. https://doi.org/10.1016/j.fuel.2018.01.115.
Meng, S., Liu, H., Yang, Q., 2019. Exploration and practice of carbon sequestration realized by CO_2 waterless fracturing. Energy Proc. 158, 4586–4591. https://doi.org/10.1016/j.egypro.2019.01.750.
Ma, D., Cheng, C., Ding, C., et al., 2021. Comparisons of fracturing mechanism of tight sandstone using liquid CO_2 and water. J. Nat. Gas Sci. Eng. 94, 104108. https://doi.org/10.1016/j.jngse.2021.104108.
Muther, T., Qureshi, H.A., Syed, F.I., et al., 2022. Unconventional hydrocarbon resources: geological statistics, petrophysical characterization, and field development strategies. J. Pet. Explor. Prod. Technol. 12, 1463–1488. https://doi.org/10.1007/s13202-021-01404-x.
Pillai, U., Heider, Y., Markert, B., 2018. A diffusive dynamic brittle fracture model for heterogeneous solids and porous materials with implementation using a user-element subroutine. Comput. Mater. Sci. 153, 36–47. https://doi.org/10.1016/j.commatsci.2018.06.024.
Rummel, F., 1987. Fracture mechanics approach to hydraulic fracturing stress measurements. In: Atkinson, B.K. (Ed.), Fracture Mechanics of Rock. E-Publishing Inc, New York, pp. 217–240. https://doi.org/10.1016/B978-0-12-066266-1.50011-9.
Rayudu, N.M., Tang, X., Singh, G., 2019. Simulating three dimensional hydraulic fracture propagation using displacement correlation method. Tunn. Undergr. Space Technol. 85 (3), 84–91. https://doi.org/10.1016/j.tust.2018.11.010.
Song, Y., Li, Z., Jiang, Z., et al., 2017. Progress and development trend of unconventional oil and gas geological research. Petrol. Explor. Dev. 44 (4), 675–685. https://doi.org/10.1016/S1876-3804(17)30077-0.
She, C., Peng, H., Yang, J., et al., 2023. Experimental study on the true triaxial fracturing of tight sandstone with supercritical CO_2 and slickwater. J. Petrol. Sci. Eng. 228, 211977. https://doi.org/10.1016/j.geoen.2023.211977.
Uzun, O., Kazemi, H., 2021. Assessment of enhanced oil recovery by osmotic pressure in unconventional reservoirs: application to Niobrara chalk and Codell sandstone. Fuel 306 (1), 121270. https://doi.org/10.1016/j.fuel.2021.121270.
Verdon, J.P., Kendall, J.M., Maxwell, S.C., 2010. A comparison of passive seismic monitoring of fracture stimulation from water and CO_2 injection. Geophysics 75 (3), MA1–MA7. https://doi.org/10.1190/1.3377789.
Wang, J., Wang, Z., Sun, B., et al., 2019a. Optimization design of hydraulic parameters for supercritical CO_2 fracturing in unconventional gas reservoir. Fuel 235, 795–809. https://doi.org/10.1016/j.fuel.2018.08.078.
Wang, M., Chen, S., Lin, M., 2019b. Enhancing recovery and sensitivity studies in an unconventional tight gas condensate reservoir. Petrol. Sci. 15, 305–318. https://doi.org/10.1007/s12182-018-0220-7.
Wang, Y., Ju, Y., Chen, J., et al., 2019c. Adaptive finite element–discrete element analysis for the multistage supercritical CO_2 fracturing and microseismic modelling of horizontal wells in tight reservoirs considering pre-existing fractures and thermal-hydro-mechanical coupling. J. Nat. Gas Sci. Eng. 61, 251–269. https://doi.org/10.1016/j.jngse.2018.11.022.
Wang, K., Pan, H., Fujii, Y., 2024. Study on energy distribution and attenuation of CO_2 fracturing vibration from coal-like material in a new test platform. Fuel 356, 129584. https://doi.org/10.1016/j.fuel.2023.129584.
Wang, C., Zhang, X., 2018. Distribution rule of the in situ stress state and its influence on the permeability of a coal reservoir in the southern Qinshui Basin, China. Arab J Geosci 11, 586. https://doi.org/10.1007/s12517-018-3938-z.
Yan, H., Zhang, J., Li, M., et al., 2019. New insights on supercritical CO_2 fracturing coal mass: a staged analysis method. Greenh Gases 9 (6), 1266–1275. https://doi.org/10.1002/ghg.1926.
Yang, Z., Zhang, Z., Nie, H., 2020. Al_2O_3-H_2O numerical simulation of flow characteristics of nanofluids in tubes. J. Hunan Univ. Sci. Technol. (Nat. Sci. Ed.) 35 (2), 90–94 (in Chinese).
Yan, H., Zhang, J., Zhou, N., et al., 2021. Quantitative characterization of crack propagation behavior under the action of stage-by-stage fracturing induced by Sc-CO_2 fluid. Eng. Fract. Mech. 256, 107984. https://doi.org/10.1016/j.engfracmech.2021.107984.
Zhu, W., Wei, C., Li, S., et al., 2013. Numerical modeling on destress blasting in coal seam for enhancing gas drainage. Int J Rock Mech Min 59, 179–190. https://doi.org/10.1016/j.ijrmms.2012.11.004.
Zhang, X., Lu, Y., Tang, J., et al., 2016. Experimental study on fracture initiation and propagation in shale using supercritical carbon dioxide fracturing. Fuel 190 (15), 370–378. https://doi.org/10.1016/j.fuel.2016.10.120.
Zhao, Z., Li, X., He, J., et al., 2018. A laboratory investigation of fracture propagation induced by supercritical carbon dioxide fracturing in continental shale with interbeds. J. Pet. Sci. Eng. 166, 739–746. https://doi.org/10.1016/j.petrol.2018.03.066.
Zhou, S., Luo, X., Jiang, N., et al., 2021. Ground vibration characteristics of carbon dioxide phase transition fracturing: an in-situ test. Bull. Eng. Geol. Environ. 80, 9029–9047. https://doi.org/10.1007/s10064-021-02479-w.
Zhou, D., Zhang, G., Zhao, P., et al., 2018. Effects of post-instability induced by supercritical CO_2 phase change on fracture dynamic propagation. J. Pet. Sci. Eng. 162, 358–366. https://doi.org/10.1016/j.petrol.2017.12.066.
Zhao, X., Huang, B., Xu, J., 2019. Experimental investigation on the characteristics of fractures initiation and propagation for gas fracturing by using air as fracturing fluid under true triaxial stresses. Fuel 236 (15), 1496–1504. https://doi.org/10.1016/j.fuel.2018.09.135.
Zhang, C.P., Cheng, P., Lu, Y.Y., et al., 2020. Experimental evaluation of gas flow characteristics in fractured siltstone under various reservoir and injection conditions: an application to CO_2-based fracturing. Geomech. Geophys. Geo-energ. Geo-resour. 6, 23. https://doi.org/10.1007/s40948-020-00145-1.
Zhu, W., Zhang, X., Liu, S., et al., 2022. An experimental apparatus for supercritical CO_2 fracturing of shale: system design and application tests. J. Nat. Gas Sci. Eng. 103, 104656. https://doi.org/10.1016/j.jngse.2022.104656.